

# Unsupervised Deep Unrolled Reconstruction Using Regularization by Denoising

Peizhou Huang, Chaoyi Zhang, Xiaoliang Zhang, Xiaojuan Li, Liang Dong, Leslie Ying

**Abstract**—Deep learning methods have been successfully used in various computer vision tasks. Inspired by that success, deep learning has been explored in magnetic resonance imaging (MRI) reconstruction. In particular, integrating deep learning and model-based optimization methods has shown considerable advantages. However, a large amount of labeled training data is typically needed for high reconstruction quality, which is challenging for some MRI applications. In this paper, we propose a novel reconstruction method, named DURED-Net, that enables interpretable unsupervised learning for MR image reconstruction by combining an unsupervised denoising network and a plug-and-play method. We aim to boost the reconstruction performance of unsupervised learning by adding an explicit prior that utilizes imaging physics. Specifically, the leverage of a denoising network for MRI reconstruction is achieved using Regularization by Denoising (RED). Experiment results demonstrate that the proposed method requires a reduced amount of training data to achieve high reconstruction quality.

**Index Terms** — Magnetic resonance image reconstruction, deep neural network, unsupervised learning, regularization by denoising.

## I. INTRODUCTION

MAGNETIC resonance imaging (MRI) is one of the premier imaging modalities used clinically due to its ability to provide anatomic details and superior soft-tissue contrast. However, a major challenge of MRI is its long acquisition time. Many techniques have been developed to increase the MRI speed, such as parallel imaging [1, 2]. Over the past decades, compressed sensing (CS) [3] has become an important technique to accelerate MRI. Many optimization methods with different regularization models have been developed for CS-MRI, such as learned dictionaries [4, 5], low-rankness [6, 7], and manifold models [8, 9], leading to robust and practical algorithms with excellent performance.

In the past few years, deep learning [10] techniques provide excellent end-to-end learning capabilities in the field of computer vision, ranging from denoising, deblurring, to super-resolution and image restoration. Inspired by that success, deep neural networks have been applied to MRI reconstruction from

reduced measurements [11-17]. Different from CS-MRI methods which solve the ill-posed inverse problem with mathematical constraints using optimization algorithms, these deep learning-based methods use a large amount of labeled training data to learn the complicated relationship between the aliased image and the ground truth image, which is represented with standard convolutional neural networks (CNN). These deep learning-based methods are able to address the limitations that the CS-MRI methods typically need sophisticated priors with hand-tuned parameters and iterative algorithms with long runtime. However, it can be challenging to obtain a large amount of labeled training data in certain applications such as dynamic imaging, relaxometry imaging, and diffusion imaging.

In the meanwhile, several studies have applied deep learning to model-based optimization methods in MR image reconstruction by unrolling the iterative optimization to a deep network [18-20]. For example, Yang et al [18] introduced a single-coil MR reconstruction method by unrolling the alternating direction method of multipliers (ADMM) algorithm to several self-defined layers to learn the regularization parameters in ADMM. Hammernik et al [19] unrolled the variational models for iterative reconstruction to a deep network to learn the regularization parameters, as well as the nonlinear operators. Zhang et al [20] unrolled the iterations in the ISTA algorithm to layers of networks to learn the image transformation and parameters. These unrolling-based methods usually demand less training data due to the physics-driven architecture and the reduced number of training parameters compared with the standard networks.

More recently, several methods have been proposed to incorporate data consistency as additional information in the deep learning-based reconstruction methods. Those methods leverage the benefits of both the physical model and standard network structures. They took advantage of CNN's powerful capability of learning the prior model using a deep architecture and integrated it with the model-based inverse problem [21-24]. For example, Aggarwal et al [21] combined a CNN denoiser with the conjugate gradient optimization scheme for MRI reconstruction. Schlemper et al [22] created a cascade architecture that alternates between an intermediate de-aliasing

This work was supported by the NIH/NIAMS R01 AR077452.

P. Huang and X. Zhang are with the Biomedical Engineering Department, State University of New York at Buffalo, Buffalo, NY 14260 USA.

C. Zhang is with Electrical Engineering Department, State University of New York at Buffalo, Buffalo, NY 14260 USA.

X. Li is with Program of Advanced Musculoskeletal Imaging (PAMI), Cleveland Clinic, Cleveland, Ohio 44103, USA

D. Liang is with Paul C. Lauterbur Research Center for Biomedical Imaging, SIAT, CAS, Shenzhen 518055, P.R.China

L. Ying is with the Biomedical Engineering Department and Electrical Engineering Department, State University of New York at Buffalo, Buffalo, NY 14260 USA.

CNN and data consistency for dynamic MRI reconstruction. Eo et al [23] applied the image domain CNN and k-space CNN with interleaved data consistency in MRI reconstruction that allows outstanding detail restoration. Cheng et al [24] proposed to embed both data consistency and prior information in the network such that both can be learned jointly. A more comprehensive summary of deep learning-based reconstruction algorithms can be found in [25].

However, the above-mentioned deep learning-based reconstruction methods require ground truth images as the labeled training data. Some methods have been developed to use the undersampled data only for unsupervised learning [26-35]. Among these methods, some generate paired training data from the undersampled data [26-28], some use the Generative Adversarial Networks (GAN) to guide the training process [29-32], and others use statistical properties of the data to reconstruct the image [33-35]. In particular, Noise2Noise [36], an unsupervised CNN-based denoiser, has been used to reconstruct clean images from aliased images without ground-truth training images. Built upon the success of plug-and-play methods that solve a regularized inverse problem by sequentially applying image denoising with high-performing denoisers, RARE [37] uses a pre-trained Artifacts2Artifacts network (equivalent to Noise2Noise in [36]) as the denoiser to perform MR image reconstruction with unsupervised learning. However, the limitation of RARE is that the image reconstruction quality heavily relies on the pre-trained CNN denoiser whose training requires a large training size. As a result, the RARE reconstruction quality is not optimal.

In this paper, we propose a novel deep unrolled unsupervised method powered by regularization by denoising (RED) [38] for MRI reconstruction, named DURED-Net. The method integrates Noise2Noise with RED. Unlike the existing unsupervised methods for inverse problems, RARE, where the denoising network is pre-trained with unsupervised learning and then plugged into the iterative procedures of RED directly, the denoising engine in the proposed method is trained along with the unrolled ADMM iterations of RED so that the network parameter depends not only on the training samples but also on the imaging model of the inverse problem. Such integrated training makes unsupervised learning to be more efficient for the specific imaging model. In addition, the ADMM iteration is also treated as an unrolled network whose parameter is learned using the training data. In particular, although RARE also combines the Noise2Noise network with RED, our proposed method is superior in that it not only leverages the unsupervised learning capability of Noise2Noise but also unrolls the ADMM-based iterations of RED as another network and learns the parameters of both networks jointly during the training process. As a result, the proposed method demonstrates improved reconstruction quality, alleviated overfitting issues, lessened requirements on training size, and reduced sensitivity to network hyperparameters (e.g., layers, etc.).

This paper is organized as follows. Section II presents the background of Noise2Noise, an unsupervised method for MR image reconstruction, and RED. Section III presents the

proposed unsupervised learning method and illustrates each module of the network architecture. Section IV describes the datasets used for evaluation and the implementation details of the proposed model. In section V, we present promising results compared to other supervised/unsupervised methods. The conclusion is presented in Section VI.

## II. BACKGROUND

### A. Regularizing image reconstruction with denoising

In the context of compressed sensing, the purpose is to reconstruct the latent image  $\mathbf{x}$  from its undersampled measurement  $\mathbf{y} = \mathbf{A}\mathbf{x}$ , where  $\mathbf{A}$  is a measurement matrix that contains the undersampling process and Fourier transform. Since the problem is ill-posed, regularization needs to be adopted to reconstruct the latent image. Mathematically, this entails solving an optimization problem by minimizing this objective function:

$$\hat{\mathbf{x}} = \arg \min_{\mathbf{x}} \frac{1}{2} \|\mathbf{A}\mathbf{x} - \mathbf{y}\|^2 + \lambda \rho(\mathbf{x}). \quad (1)$$

where  $\frac{1}{2} \|\mathbf{A}\mathbf{x} - \mathbf{y}\|^2$  represents data consistency,  $\rho(\mathbf{x})$  the regularization function, and  $\lambda$  the regularization parameter.

As many denoising algorithms have demonstrated their success in the past years, several methods have been proposed to leverage denoising algorithms in image reconstruction [38-39]. Among these works, Regularization by Denoising (RED) [38] demonstrates its advantages of flexibility in using the denoising engine for regularization in inverse problems. RED constructs an explicit formulation as the regularization function with an arbitrary image denoiser:

$$\hat{\mathbf{x}} = \arg \min_{\mathbf{x}} \frac{1}{2} \|\mathbf{A}\mathbf{x} - \mathbf{y}\|^2 + \frac{1}{2} \lambda \mathbf{x}^T (\mathbf{x} - f(\mathbf{x})). \quad (2)$$

where  $f(\cdot)$  is a denoiser engine. There are two important properties in RED: (1) The gradient of the prior is given by  $\nabla \rho(\mathbf{x}) = \mathbf{x} - f(\mathbf{x})$ , which avoids differentiating the denoisers function. (2)  $\rho(\mathbf{x})$  is a convex functional. With the development of plug-and-play methods, the denoiser engine can be plugged in an iterative scheme in different ways. All those schemes involve a data consistency term related subproblem and a regularization term that contains the denoiser engine related to the denoising subproblem. Consequently, many highly effective denoising algorithms can be used to solve reconstruction problems.

Recently, with the powerful denoising ability of the neural network, we can see that the neural network can be as a denoiser prior and plugged in an iterative scheme in different ways [21, 37]. However, most of these existing works relied on a pre-trained network where the network parameters are pre-learned and not changed along with the iterative procedure of the corresponding algorithm.

### B. Deep learning reconstruction using unrolling

Deep learning has also been used in MRI reconstruction recently to learn the mapping between the undersampled k-space data (input)  $\hat{\mathbf{x}}_i$  and the ground truth image from fully sampled data (target)  $\mathbf{x}_{GT}$  using a large number of training pairs

$(\hat{\mathbf{x}}_i, \mathbf{x}_{GT})$ . However, the deep learning methods cannot guarantee data consistency nor utilize sophisticated priors for improved performance. As a consequence, there have been several works that unroll the iterative procedures in MRI image reconstruction to a deep network with a certain architecture so that the regularization functions and parameters that used to be fixed become learnable using the training data, such as ADMM-net [18], variational-net [19], ISTA-net [20], and MoDL [21].

These unrolling-based methods have the advantage of utilizing the MR physical model while embracing the benefit of a deep network. It has been shown that decoupling the data consistency term and regularization term allows a wide variety of existing inverse algorithms to be combined with a neural network. The unrolling-based method commonly starts from a regularized optimization algorithm for Eq. (1) but unrolls iterations of the algorithm to stages of the neural network. The method overcomes the issue of selecting regularization functions and parameters. For example, ADMM-Nets unroll the ADMM iterations to a deep network from the following minimization problem

$$\hat{\mathbf{x}} = \arg \min_{\mathbf{x}} \frac{1}{2} \|\mathbf{A}\mathbf{x} - \mathbf{y}\|^2 + \sum_{l=1}^L \lambda_l g(\mathbf{D}_l \mathbf{x}). \quad (3)$$

It learns the nonlinear transforms  $\mathbf{D}_l$ , regularization function  $g(\cdot)$ , and parameters  $\lambda_l$  using training data.

### C. Noise2Noise

Deep learning has shown success in image denoising [36, 40]. In supervised learning, the network learns the relationship

between the noisy image (input)  $\hat{\mathbf{x}}_1^i$  and its clean counterpart (target)  $\mathbf{x}_{GT}^i$  using a large number of training pairs  $(\hat{\mathbf{x}}_1^i, \mathbf{x}_{GT}^i)$  by minimizing the mean squared error (L2):

$$\arg \min_{\theta} \frac{1}{n} \sum_{i=1}^n \|f(\hat{\mathbf{x}}_1^i, \theta) - \mathbf{x}_{GT}^i\|^2. \quad (4)$$

where  $f(\hat{\mathbf{x}}_1^i, \theta)$  is the denoising neural network with network parameter  $\theta$ ,  $n$  is the total number of training samples. Because the clean image is not always available, Noise2Noise has been proposed as an unsupervised learning method without the need for the ground-truth clean image in training. It replaces the noisy-clean training pairs with noisy-noisy ones when training the network:

$$\arg \min_{\theta} \frac{1}{n} \sum_{i=1}^n \|f(\hat{\mathbf{x}}_1^i, \theta) - \hat{\mathbf{x}}_2^i\|^2. \quad (5)$$

where  $\hat{\mathbf{x}}_1^i$  and  $\hat{\mathbf{x}}_2^i$  are both noisy images of the same clean one. It was demonstrated in [36] that such training is equivalent to training with the ground truth images when the following conditions are satisfied:

1. The number of training sample  $n$  is infinite;
2. The conditioned expectation  $\mathbb{E}\{\hat{\mathbf{x}}_2^i | \hat{\mathbf{x}}_1^i\} = \mathbf{x}_{GT}^i$ ;
3.  $\hat{\mathbf{x}}_1^i$  and  $\hat{\mathbf{x}}_2^i$  are from the same image corrupted by independent noise of the same distribution.

That is, minimizing the loss function of Eq. (5) is the same as that of Eq. (4) when the above conditions are satisfied.

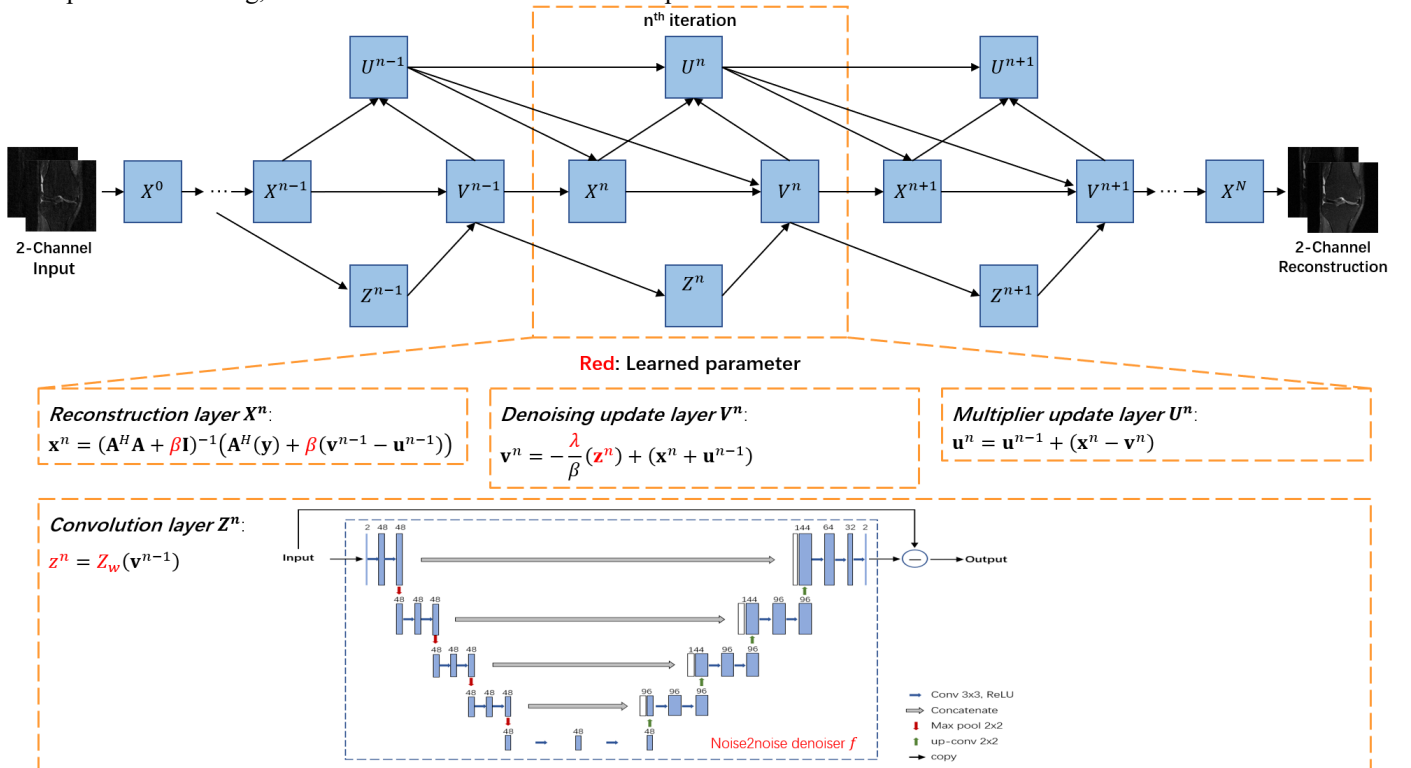


Figure 1. The proposed unsupervised learning framework for MRI image reconstruction. The network structure is defined over the iterative procedures of Eq. (14). The four procedures correspond to four layers, which are named as reconstruction layer  $X^n$ , Convolution layer  $Z^n$ , Denoising update layer  $V^n$ , and Multiplier update layer  $U^n$ . The variables in red are learned during training. The graph illustrates the unrolled architecture with 3 modules in one training epoch.

### III. PROPOSED METHOD

#### A. Problem formulation

In RED, the denoiser  $f(\cdot)$  is plugged into the optimization procedure of Eq. (1), and the splitting variable method is adopted to decouple the data consistency term and a regularization term. Using ADMM [41], Eq. (1) is first reformulated as a constrained optimization problem by introducing an auxiliary variable  $\mathbf{z}$ :

$$(\hat{\mathbf{x}}, \hat{\mathbf{v}}) = \arg \min_{\mathbf{x}, \mathbf{v}} \frac{1}{2} \|\mathbf{A}\mathbf{x} - \mathbf{y}\|^2 + \lambda \frac{1}{2} \mathbf{v}^T (\mathbf{v} - f(\mathbf{v})) \text{ s.t. } \mathbf{x} = \mathbf{v}. \quad (6)$$

Then solving Eq. (6) is equivalent to minimizing the augmented Lagrangian function:

$$\mathcal{L}(\mathbf{x}, \mathbf{v}, \mathbf{u}) = \frac{1}{2} \|\mathbf{A}\mathbf{x} - \mathbf{y}\|^2 + \lambda \frac{1}{2} \mathbf{v}^T (\mathbf{v} - f(\mathbf{v})) + u^T (\mathbf{x} - \mathbf{v}) + \frac{\beta}{2} \|\mathbf{x} - \mathbf{v}\|^2. \quad (7)$$

Finally, finding the minimum for  $\mathcal{L}$  can be solved by a sequence of subproblems in the form

$$\begin{cases} \mathbf{x}^n = \arg \min_{\mathbf{x}} \left\{ \frac{1}{2} \|\mathbf{A}\mathbf{x} - \mathbf{y}\|_2^2 + \frac{\beta}{2} \|\mathbf{x} - \tilde{\mathbf{x}}^{n-1}\|_2^2 \right\} \\ \mathbf{v}^n = \arg \min_{\mathbf{v}} \left\{ \frac{\beta}{2} \|\mathbf{v} - \tilde{\mathbf{v}}^{n-1}\|_2^2 + \frac{\lambda}{2} \mathbf{v}^T (\mathbf{v} - f(\mathbf{v}^{n-1})) \right\} \\ \mathbf{u}^n = \mathbf{u}^{n-1} + (\mathbf{x}^n - \mathbf{v}^n), \end{cases} \quad (8)$$

where  $n$  refers to the iteration index in ADMM,  $u^n$  is the scaled Lagrange multiplier,  $\tilde{\mathbf{x}}^{n-1} = \mathbf{v}^{n-1} - \mathbf{u}^{n-1}$  and  $\tilde{\mathbf{v}}^{n-1} = \mathbf{x}^n + \mathbf{u}^{n-1}$  are the intermediate variables.

1) *Solving subproblem  $\mathbf{x}^n$  in Eq. (8)*: The subproblem of  $\mathbf{x}^n$  can be solved analytically by:

$$\mathbf{x}^n = (\mathbf{A}^H \mathbf{A} + \beta \mathbf{I})^{-1} (\mathbf{A}^H (\mathbf{y}) + \beta (\mathbf{v}^{n-1} - \mathbf{u}^{n-1})). \quad (9)$$

It typically takes a few conjugate gradient iterations to approximate the solution in Eq. (9).

2) *Solving subproblem  $\mathbf{v}^n$  in Eq. (8)*: In RED, it was shown that for any image denoiser, the gradient of RED regularization obeys the gradient rule that

$$\nabla \rho(\mathbf{x}) = \mathbf{x} - f(\mathbf{x}). \quad (10)$$

Then, any minimization of  $v^n$  in (8) must yield  $\nabla v^n = 0$ , so that the gradient of  $v^n$  can be represented in the form of

$$\lambda (\mathbf{v}^n - f(\mathbf{v}^{n-1})) + \beta (\mathbf{v}^n - \mathbf{x}^n - \mathbf{u}^{n-1}) = 0. \quad (11)$$

Interestingly, Eq. (11) implies that the minimization of  $v^n$  contains the denoising residual from  $\mathbf{v}^{n-1}$ . Therefore, in this paper, a CNN is constructed to learn such deep denoising residual in the form of

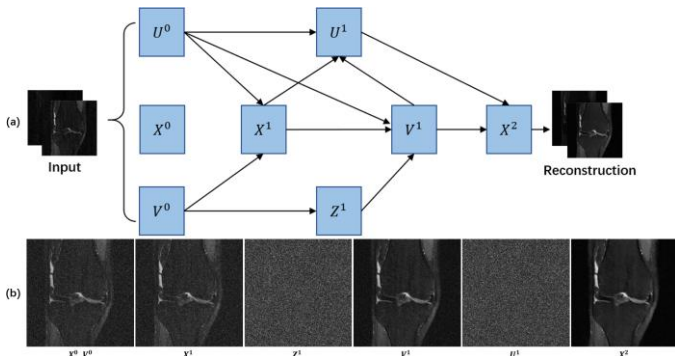


Figure 2. Simplified network. (a) Network architecture with two modules. (b) Intermediate outputs of layers in (a).

$$\mathbf{z}^n = Z_w(\mathbf{v}^{n-1}) = \mathbf{v}^n - f(\mathbf{v}^{n-1}). \quad (12)$$

where  $Z_w$  denotes the CNN with the learned network parameter  $w$ . Therefore, CNN can be learned along with solving subproblems  $\mathbf{v}^n$  in ADMM by taking the input  $\mathbf{v}^{n-1}$ , and the solution of  $\mathbf{v}^n$  in (8) can be represented directly as

$$\mathbf{v}^n = -\frac{\lambda}{\beta} (\mathbf{z}^n) + (\mathbf{x}^n + \mathbf{u}^{n-1}). \quad (13)$$

#### 3) Updating $\mathbf{u}^n$ using Eq. (8).

Combining the above three subproblems, the solution to Eq. (8) at the  $n$ -th iteration is updated as follows:

$$\begin{cases} \mathbf{X}^n: \mathbf{x}^n = (\mathbf{A}^H \mathbf{A} + \beta \mathbf{I})^{-1} (\mathbf{A}^H (\mathbf{y}) + \beta (\mathbf{v}^{n-1} - \mathbf{u}^{n-1})) \\ \mathbf{Z}^n: \mathbf{z}^n = Z_w(\mathbf{v}^{n-1}) \\ \mathbf{V}^n: \mathbf{v}^n = -\frac{\lambda}{\beta} (\mathbf{z}^n) + (\mathbf{x}^n + \mathbf{u}^{n-1}) \\ \mathbf{U}^n: \mathbf{u}^n = \mathbf{u}^{n-1} + (\mathbf{x}^n - \mathbf{v}^n). \end{cases} \quad (14)$$

#### B. Network architecture

We unroll the iterations in Eq. (14) to a deep neural network such that all the network parameters can be learned through training instead of being selected empirically. The architecture of the deep network is shown in Figure 1. The four steps in Eq. (14) are represented as four layers in the neural network including the reconstruction layer  $\mathbf{X}^n$ , the convolution layer  $\mathbf{Z}^n$ , the denoising update layer  $\mathbf{V}^n$ , and the multiplier update layer  $\mathbf{U}^n$ . The  $n$ -th iteration corresponds to the  $n$ -th module of the deep network enclosed with the dashed box. Figure 1 shows an example with three iterations in one training epoch. All parameters  $\{\lambda, \beta\}$  and the denoiser  $f$  that are predetermined in the original RED-ADMM algorithm are now learned through training in the proposed method.

Next, we provide details for each module of the proposed DURED-Net.

1) *Reconstruction layer  $\mathbf{X}^n$* : This layer reconstructs an image of the current iteration or layer under the given  $\{\mathbf{v}^{n-1}, \mathbf{u}^{n-1}\}$  according to the first item of Eq. (14),  $\mathbf{X}^n: \mathbf{x}^n = (\mathbf{A}^H \mathbf{A} + \beta \mathbf{I})^{-1} (\mathbf{A}^H (\mathbf{y}) + \beta (\mathbf{v}^{n-1} - \mathbf{u}^{n-1}))$ . In the input layer  $x^0, v^0$  are initialized in two channels representing the real and imaginary parts of the zero-filled Fourier reconstruction, and  $\mathbf{u}^0$  is initialized to zero. For  $n \geq 1$ , the input and output of  $\mathbf{x}^n$  are both complex-valued data. The hyper-parameter  $\beta$  is set as a learnable parameter, which is initialized to 10.

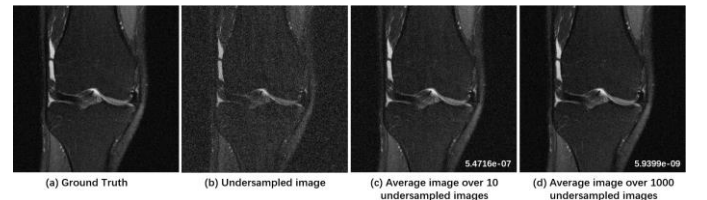


Figure 3. Property of the proposed random undersampling pattern. The nMSE is shown at the bottom right corner. From left to right are (a) ground truth; (b) aliased image from undersampled weighted k-space; (c)-(d) images averaged over 10 and 1000 aliased images from randomly undersampled data, respectively.

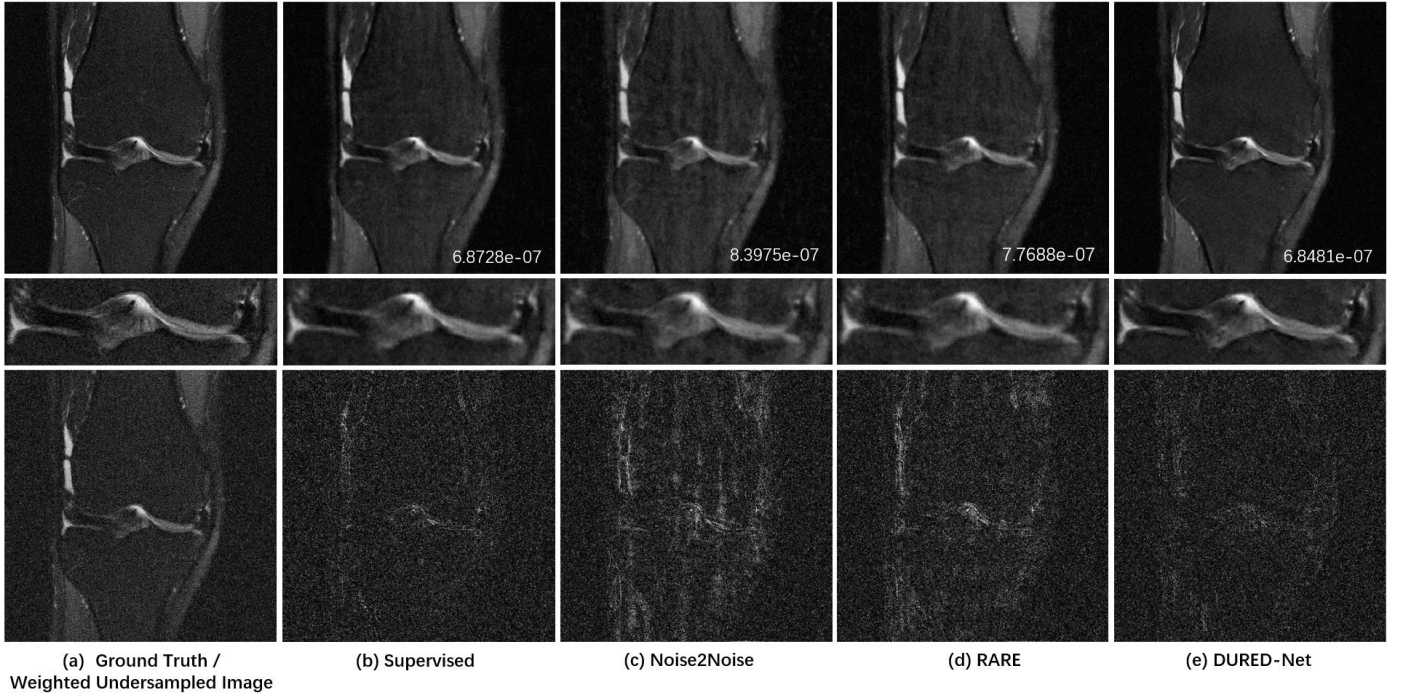


Figure 4. Comparison of the proposed DURED-Net with other networks. From left to right: Ground truth (top) and aliased image (bottom) as the network input, reconstructions with (b) supervised and unsupervised training using (c) Noise2Noise, (d) RARE, and (e) DURED-Net. From top to bottom: reconstructed images, regions of interest (ROI), and differences (enlarged 4 times) from the ground truth, all on the same scale. The nMSEs are shown at the bottom right corner.

2) **Convolution layer  $Z^n$** : This layer performs a convolution operation to find the deep denoising residual of  $\mathbf{v}^{n-1}$  according to the second term of Eq. (14),  $Z^n: \mathbf{z}^n = Z_w(\mathbf{v}^{n-1})$ . The network adopts a subtract structure between the input  $\mathbf{v}^{n-1}$  and the denoiser network. Therefore, the denoising network  $f_\theta$  is learned implicitly inside  $Z_w$ . We used a U-net [42] structure in the convolution layer  $Z^1$  in our DURED-Net as shown in Figure 1. Because standard CNNs processes real-valued data, both the input and output of  $Z_w$  have two channels representing the real and imaginary parts of the complex data.

3) **Denoising update layer  $V^n$** : This layer is to solve the denoising constrained problem to the actual minimization with the deep denoising residual  $\mathbf{z}^n$  with known  $\{x^n, u^{n-1}\}$  according to the third item  $V^n$  in Eq. (14). The two-channel output of the convolution layer  $Z^n$  is combined into a single-channel input of complex value and used as the input of  $V^n$ . The hyper-parameter  $\lambda$  is set as a learnable parameter, which is initialized to 10.

4) **Multiplier update layer  $U^n$** : This layer is used to update the Lagrange multiplier  $u^n$  under the last term  $U^n$  in Eq. (14).

In the final reconstruction layer  $X^n$ , the complex output image is decomposed into the real and imaginary channels to calculate the  $L_2$  loss.

Considering the increased memory and computational costs with more layers, here we choose a two-module network as shown in Figure 2a, where the initial variable  $X^0$  and  $V^0$  are zero-filled input images from the undersampled data,  $U^0$  is initialized to zeros. Networks with more modules are discussed in Section V. Figure 2b shows the intermediate output of each layer, where  $\{X^i\}_{i=1}^2$  is the updated reconstruction,  $V^1$  is the updated image in the regularization,  $Z^1$  is the deep learned

residual structure that is used for updating  $V^1$ , and  $U^1$  is the updated dual variable.

It is worth noting that the input and output of the network, which are the zero-filled images from randomly undersampled data with different sampling patterns, meet conditions #2 and #3 of Noise2Noise for unsupervised training. The details of how to meet the conditions are elaborated further in Section III.C. As a result, similar to Noise2Noise, the proposed network can also generate a desired Nyquist-sampled image while using unlabeled undersampled training data only for training. This is significant in many dynamic imaging applications where the Nyquist-sampled data are impossible to acquire due to motion. The key benefit of the proposed scheme over [37] is that the denoising layer is not pre-trained but is learned jointly with other layers with data consistency constraints from the forward imaging model. The denoising layer is updated using the training data in each epoch so that the entire network performs better than the one with a pre-trained denoiser.

### C. Design of sampling pattern

Recall in Section I.C, there are three conditions for the unsupervised training in Noise2Noise to perform well [36]. In our context of image reconstruction, condition #2 means that if we take an infinite number of aliased images that are from independently generated random samples and average them (to approximate the expectation), then the average should be equal to the aliasing-free, ground truth image. Condition #3 means the k-space of an image is undersampled by two different sampling patterns that are randomly generated with the same probability density function. The second condition requires that the expectation of the random undersampling k-space spectrum be equal to the full sampling of the spectrum. To meet the

requirements, Noise2Noise used a Bernoulli sampling where each k-space location has a probability  $p(k) = e^{-\lambda|k|}$  of being selected for acquisition, where  $k$  is the k-space location, and the sampled values are further weighted by  $\frac{1}{p(k)}$ . Here, we propose an improved random sampling pattern, where the probability density function (PDF) is

$$p(k) = e^{\left(\frac{-1}{\mu}|k|\right)^\alpha} \quad (16)$$

with  $\mu$  and  $\alpha$  the parameters to control the sampling location. The sampled values are also weighted by the inverse of the PDF. The proposed sampling pattern can be used for 1D, 2D, and even higher dimensional undersampling.

Figure 3 shows an aliased image that is the zero-filled Fourier reconstruction from the k-space data with the above-introduced undersampling and the averages of 10 and 1000 such images with random sampling. The normalized mean square error (nMSE) is shown at the right bottom corner. These results demonstrate that averages of more images with different sampling patterns can better approximate the ground-truth image.

## IV. EXPERIMENTAL SETUPS

### A. Dataset

We used the raw single-coil k-space MR data from the knee fastMRI dataset [43] that is available publicly at <https://fastmri.org/>. In particular, we randomly selected 200 sagittal knee MR scans subjects and used them in the training procedure. There are out of the total 40 images for each subject, and we selected 20 central images that had the anatomy, which gave a maximum of 4000 images. Among them, 1000 images were used for training. We further selected another 20 different subjects from the same dataset with 20 central images for each subject, which gave additional 400 images for testing. The dataset with the Turbo Spin Echo sequence has parameters as shown in Table I. All images are complex-valued.

### B. Parameters

The network was trained on a patch size of  $320 \times 320$  and a mini-batch size of 8 using the Adam algorithm with the initial learning rate of  $10^{-3}$ . At each epoch, the total number of conjugate gradient iterations in the reconstruction layer  $\mathbf{X}^n$  to update  $\mathbf{x}^n$  was set to 15. The hyperparameters,  $\lambda$ , and  $\beta$  were initialized to  $\lambda = 10$  and  $\beta = 10$ .

To avoid overfitting during the training, data augmentation was used where the images were translated with a random number of pixels vertically and horizontally each time and the translation was repeated  $xx$  times. According to the Fourier transform property, the undersampled k-space data of the translated image can be calculated by multiplying a phase shift term to each k-space data point. Only simple translations were used because other types of data augmentation would change the complex-valued undersampled k-space data in a rather complicated way.

### C. Quantitative evaluation

We used nMSE to evaluate the quality of the reconstructed image quantitatively. Defining  $\mathbf{x}_{GT}$  and  $\hat{\mathbf{x}}$  to be the ground truth image and the reconstructed image, nMSE is defined as:

$$nMSE(\mathbf{x}_{GT}, \hat{\mathbf{x}}) = \frac{\|\mathbf{x}_{GT} - \hat{\mathbf{x}}\|_2^2}{\|\mathbf{x}_{GT}\|_2^2}.$$

Table I. Sequence parameters in fastMRI dataset

Parameter	Value
Echo train length	4
Matrix size	320×320
In-plane resolution	0.5mm × 0.5mm
Slice thickness	3mm
TR	2200 ~ 3000 ms
TE	27 ~ 34 ms

## V. RESULTS

### A. Comparison with competing methods

In this section, we compare DURED-Net with several deep-learning-based methods, including the supervised training with ground truth labels, and unsupervised training using Noise2Noise and RARE. Figure 4 shows the reconstructions from 5x undersampled data using four different networks. The first one is using the U-Net [42] denoising network with the ground truth images as the training labels. The second one is the Noise2Noise network trained with the aliased images only. The third one is the state-of-the-art RARE network which adds the physical models to a pre-trained Noise2Noise network. The last one is our proposed DURED-Net. For the supervised training, the same sampling pattern was used for both training and testing. All unsupervised methods used 1000 training images whose undersampling patterns were randomly generated using Eq. (16). It is worth noting that the performance of the supervised method is significantly worsened when the sampling patterns are different in training and testing. Such requirement of the same sampling patterns may present a challenge in practical MR scans because the actual sampling patterns might slightly vary between scans. The DURED-Net reconstruction shows high agreement with the ground truth image, while the images from other methods are visibly inferior with loss of sharpness and increased artifacts. The corresponding nMSEs also demonstrate the benefit of DURED-Net quantitatively.

### B. Visualization of RED Cost and the Gradient in the proposed method

To analyze the convergence behavior, we show the contour lines and the gradient field of the cost functions using contour graph visualization [44] for the proposed DURED-Net, as well as ADMM-RED based MR image reconstruction with BM3D denoiser and RARE. In RED [38], the gradient field of the cost function in Eq. (2) is

$$\mathcal{J} = \mathbf{A}^T(\mathbf{A}\mathbf{x} - \mathbf{y}) + \lambda(\mathbf{x} - f(\mathbf{x})). \quad (18)$$

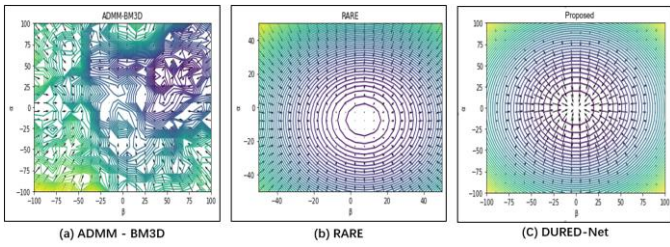


Figure 5. Contours graphs as a function of  $(\alpha, \beta)$  for different methods.

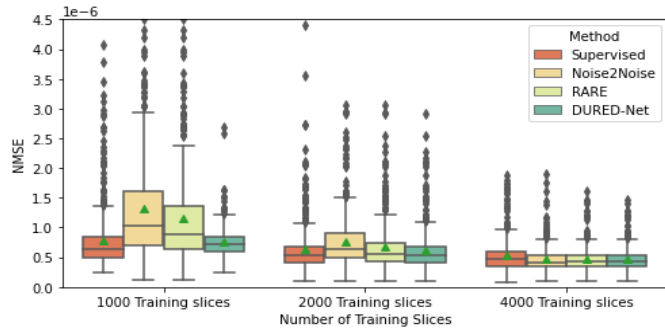


Figure 6. Boxplots of nMSEs of 400 reconstructed images when the training sizes are 1000, 2000, and 4000 images.

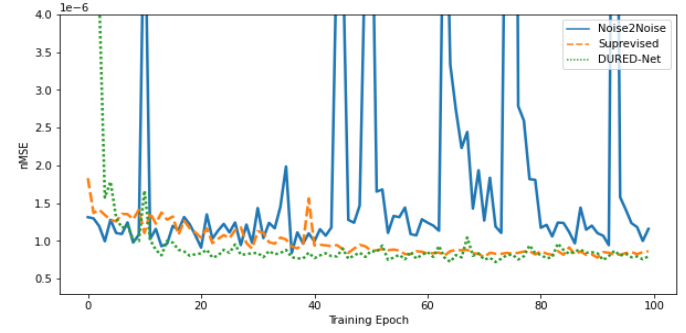


Figure 7. Training curves show nMSE versus training epoch.

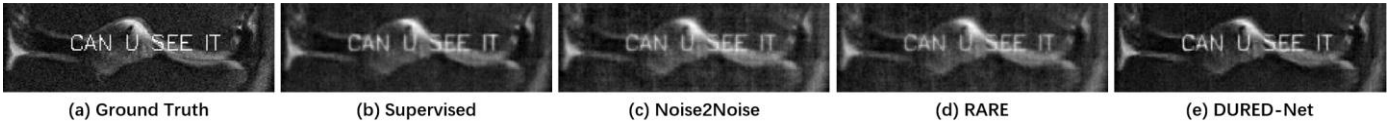


Figure 8. The reconstruction results with structured perturbations between the compared method. From (a) is the ground truth image, (b) to (e) are the reconstruction image of Supervised, Noise2noise, RARE, and proposed DURED-Net.

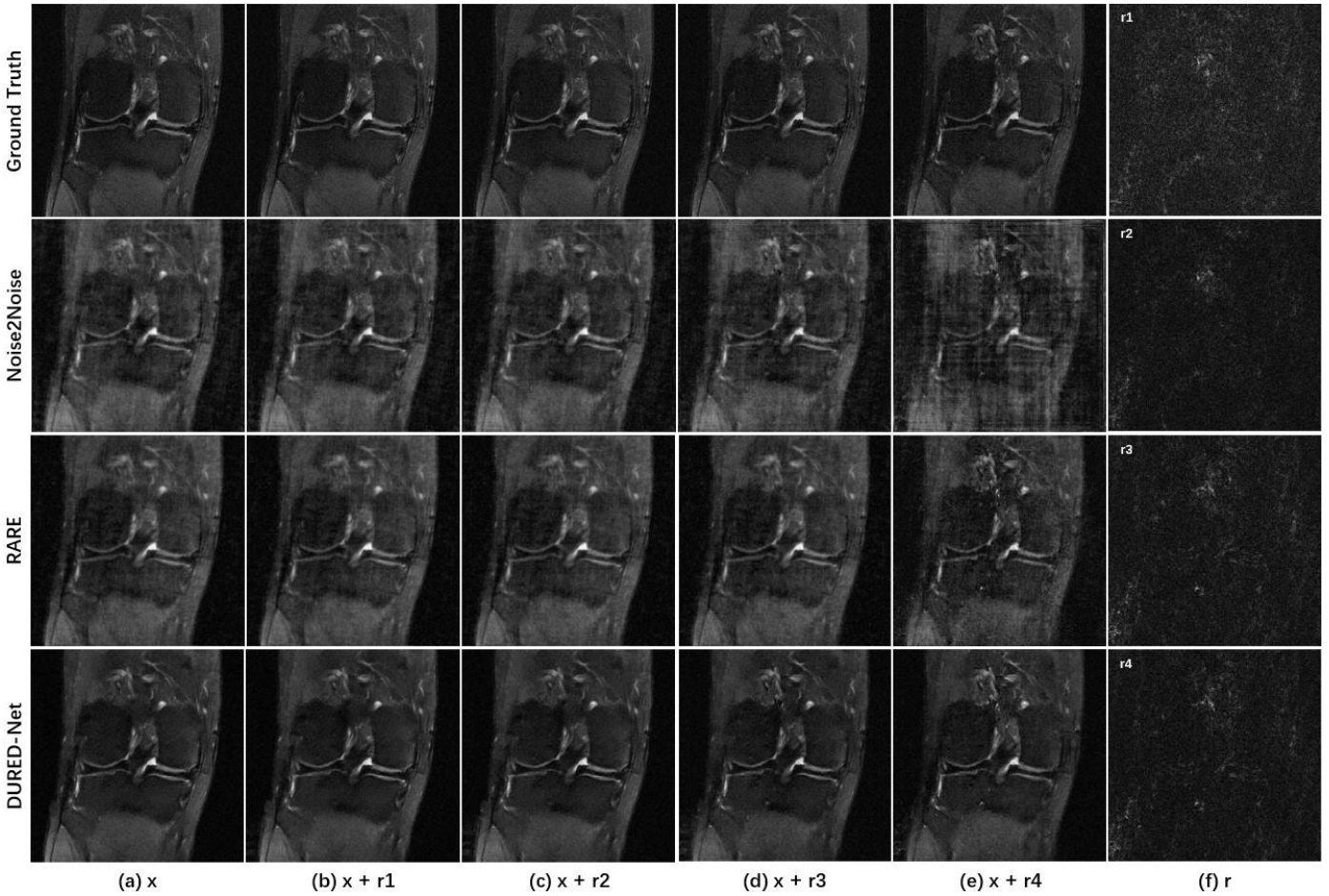


Figure 9. The ground truth images (top row), Noise2Noise (2<sup>nd</sup> row), RARE(3<sup>rd</sup> row), and DURED-Net (bottom row) reconstructions with perturbations  $r_j$  (sixth column), where  $|r_1| < |r_2| < |r_3| < |r_4|$ .

The parameter  $\lambda$  is empirically optimized in each method. Figure 5 provides a visualization of the cost functions and the gradient fields for all methods. Assuming the reconstruction is  $\hat{x}$ , two random values are added to  $\hat{x}$  in two random directions as

$$\mathbf{x}_{\alpha,\beta} = \hat{\mathbf{x}} + \alpha\boldsymbol{\varepsilon}_1 + \beta\boldsymbol{\varepsilon}_2 \quad (19)$$

where  $\boldsymbol{\varepsilon}_1$  and  $\boldsymbol{\varepsilon}_2$  are the 2D random directions following a normal distribution,  $\alpha$  and  $\beta$  are the randomly chosen values based on the size of the contour graph. The points located on the same contour have the same cost value, and the gradient field is represented by the arrows. The reconstruction is located at the origin of the plot ( $\alpha = \beta = 0$ ), and the center of the local minimum. The arrow shows the gradient descent direction that leads to a global minimum. As shown in Figure 5, ADMM-BM3D and RARE reconstructions are away from the local and global minima while the proposed DURED-Net reconstruction agrees with both the local and global optima. This is because only the proposed method updates all components of the cost function using a deep neural network.

### C. Effect of Training Size

In this section, we investigate the influence of training sizes. Figure 6 shows the boxplots of the NMSEs of reconstructions for 400 testing images. Different reconstruction methods are compared with different training sizes. When the training size is relatively small, the reconstructions of the proposed method still agree with the ground truth image well, while other methods result in larger errors. When the training size is huge, all methods have similar NMSEs, except that the supervised training is slightly worse.

Both RARE and the proposed DURED-Net perform better because of the physical model incorporated in the network, while RARE is slightly worse due to its direct adoption of a pre-trained denoiser. The proposed method is superior because both the denoiser and the ADMM-base RED are integrated and unrolled to a deep network that is updated using the training data.

The nMSEs of the reconstructions with the supervised training and unsupervised ones using Noise2Noise and DURED-net are also compared as a function of the number of training epochs, as shown in Figure 7. It is seen that the proposed method has a steady training curve while the training curves of the other two methods fluctuate with the epochs.

### D. Stability Test

We evaluate the stability of the proposed method using two different tests, as described in [45].

The first test is to add a small but visible perturbation (here we added the letters ‘‘CAN U SEE IT’’ as in [45]) to a test image.

The purpose of adding this visible perturbation is to simulate small structural changes caused by pathology that does not exist in the training image, and evaluate if these changes are still as clear in reconstruction as in the original image. As shown in Figure 8, the added letters in the proposed DURED-Net reconstruction are the sharpest of all. It demonstrates that the proposed method is able to recover structures that the network has not seen in the training images.

The second test, named tiny worst-case perturbations, is to add a small and almost-invisible perturbation in the test image and evaluate how much the perturbation deteriorates the reconstruction. We used the algorithm in [45] to generate the worst-case perturbation. The ground truth image  $x$  was perturbed with  $\{r_j\}_{j=1}^4$ ,  $|r_1| < |r_2| < |r_3| < |r_4|$ , where  $|\cdot|$  denotes L1 norm. The original image, perturbed images, and the reconstructions are shown in Figure 9. It can be seen that the perturbations corrupt the entire image of both Noise2Noise and RARE reconstructions, especially with the largest perturbation, whereas the proposed DURED-Net is still able to reconstruct the images faithfully even with large perturbations. The above instability tests demonstrate that the proposed DURED-Net is robust to imperfections during the training.

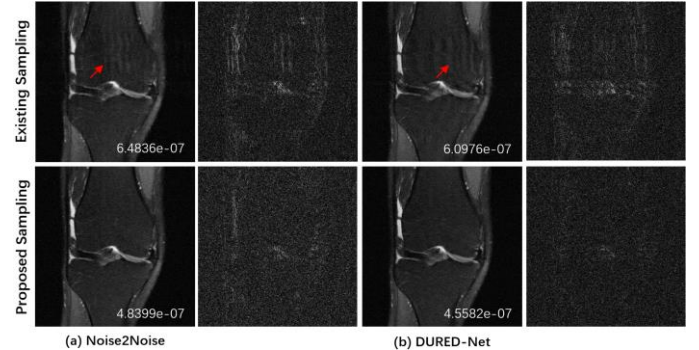


Figure 10. Reconstructions with 1D undersampling ( $3\times$ ) patterns were generated using the method in [36] (top) and the proposed DURED-Net (bottom). (a) The reconstruction of Noise2Noise. (b) The reconstruction of DURED-Net. The difference map was enlarged 4 times. The nMSEs are shown at the bottom right corner.

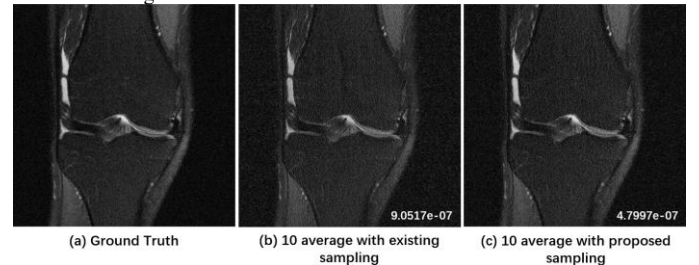


Figure 11. Comparison of the averages of 10 aliased images using two different 1D sampling patterns. The nMSEs are shown at the bottom right corner.



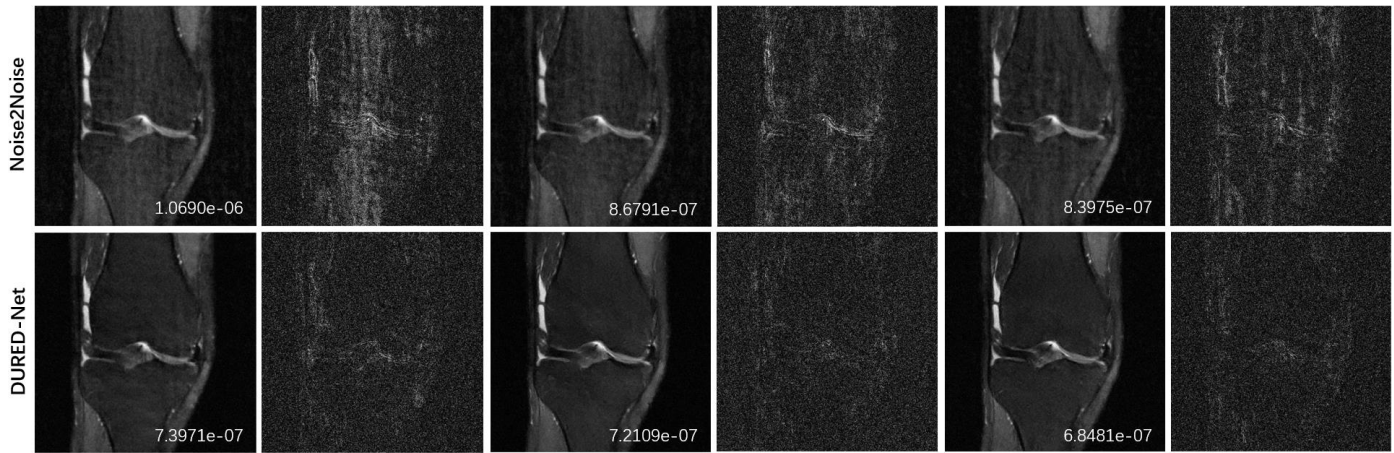


Figure 12. Noise2Noise (top) and DURED-Net (bottom) reconstructions when trained with 2, 100, and 1000 different sampling patterns, respectively. The difference map was enlarged 4 times. The nMSEs are shown at the bottom right corner.

### E. Reconstruction with 1D sampling patterns

In this section, we evaluate the performance of DURED-Net when 1D random undersampling is used. The reconstructions of Noise2Noise and DURED-Net with an undersampling factor of 3 are shown in Figure 10. The top row used the sampling scheme in [36], and the bottom row used the proposed random sampling as described in Eq. (16). A close inspection shows that the existing sampling pattern leads to the artifact as indicated by the red arrow. Whereas the proposed sampling scheme is able to spread the samples in k-space better, and the reconstruction thereby has fewer artifacts. The results also demonstrate that when the same sampling pattern is used, DURED-net is superior to Noise2Noise in reconstructing images from 1D undersampled data, which is typically used in 2D imaging. In addition, we further demonstrate the benefits of the proposed sampling in Figure 11, where the average of 10 aliased images from randomly undersampled data are compared for the existing and proposed sampling patterns. The result shows that the average using the proposed sampling is closer to the ground truth image, which suggests fewer sampling patterns are needed for training.

### F. Training with fewer sampling patterns

Finally, we investigate the effect of the number of sampling patterns in the training. Because changing to different sampling patterns is time-consuming to implement in practice, we evaluate the performance when only a few sampling patterns are used during the training. Figure 12 compares the reconstructions and their corresponding error maps when 2, 100, and 1000 sampling patterns are used in training. Both Noise2Noise and DURED-net were used for reconstruction. It can be seen that the Noise2Noise reconstruction loses more details when trained with fewer sampling patterns, whereas the DURED-net reconstruction only slightly deteriorates.

## VI. CONCLUSION

In this paper, we proposed a novel unsupervised learning method DURED-Net for MRI reconstruction from undersampled k-space data. The method effectively integrates Noise2Noise, an unsupervised learning method, with RED, a

plug-and-play method, by unrolling the underlying optimization algorithm. We also proposed an undersampling scheme to improve the performance of the reconstruction method. Results demonstrate the proposed DURED-Net can alleviate the overfitting problem in state-of-the-art methods. The method is robust to small disturbances that are absent during training. Since many different sampling patterns are used in training, the method has the benefit that reconstruction can use sampling patterns that are different from those used during training, avoiding artifacts due to sampling pattern mismatch in supervised training. The proposed method will be useful in imaging fast-moving objects where fully sampled labels are challenging to acquire.

## REFERENCES

- [1] K. P. Pruessmann, M. Weiger, M. B. Scheidegger, P. Boesiger, "SENSE: Sensitivity encoding for fast MRI," *Magn. Reson. Med.*, vol. 42, no. 5, pp. 952-62, 1999.
- [2] D. K. Sodickson and W. J. Manning, "Simultaneous acquisition of spatial harmonics (SMASH): fast imaging with radiofrequency coil arrays," *Magn. Reson. Med.*, vol. 38, no. 4, pp.591-603, 1997.
- [3] M. Lustig, D. Donoho, and J. M. Pauly, "Sparse MRI: The application of compressed sensing for rapid MR imaging," *Magn. Reson. Med.*, vol. 58, no.6, pp.1182-95, 2007.
- [4] S. Ravishanker and Y. Bresler, "MR Image Reconstruction From Highly Undersampled k-Space Data by Dictionary Learning," in *IEEE Transactions on Medical Imaging*, vol. 30, no. 5, pp. 1028-1041, 2011.
- [5] Y. Wang and L. Ying, "Compressed Sensing Dynamic Cardiac Cine MRI Using Learned Spatiotemporal Dictionary," in *IEEE Transactions on Biomedical Engineering*, vol. 61, no. 4, pp. 1109-1120, 2014.
- [6] J. P. Haldar and L. Zhi-Pei, "Spatiotemporal imaging with partially separable functions: A matrix recovery approach," 2010 *IEEE International Symposium on Biomedical Imaging: From Nano to Macro*, 2010, pp. 716-719.
- [7] J. P. Haldar, "Low-Rank Modeling of Local k-Space Neighborhoods (LORAKS) for Constrained MRI," in *IEEE Transactions on Medical Imaging*, vol. 33, no. 3, pp. 668-681, 2014.
- [8] U. Nakarmi, Y. Wang, J. Lyu, D. Liang, and L. Ying, "A Kernel-Based Low-Rank (KLR) Model for Low-Dimensional Manifold Recovery in Highly Accelerated Dynamic MRI," in *IEEE Transactions on Medical Imaging*, vol. 36, no. 11, pp. 2297-2307, 2017.
- [9] S. Poddar and M. Jacob, "Dynamic MRI Using Smoothness Regularization on Manifolds (SToRM)," in *IEEE Transactions on Medical Imaging*, vol. 35, no. 4, pp. 1106-1115, 2016.
- [10] Y. LeCun, Y. Bengio, and G. Hinton, "Deep learning," *Nature*, vol. 521, pp. 436-444, 2015.

- [11] S. Wang, Z. Su, L. Ying, X. Peng, S. Zhu, F. Liang, D. Feng, and D. Liang, "Accelerating magnetic resonance imaging via deep learning," *2016 IEEE 13th International Symposium on Biomedical Imaging (ISBI)*, 2016, pp. 514-517.
- [12] B. Zhu, J. Z. Liu, S. F. Cauley, B. R. Rosen & M. S. Rosen, "Image reconstruction by domain-transform manifold learning," *Nature*, vol. 555, pp. 487-492, 2018.
- [13] D. Lee, J. Yoo, and J. C. Ye, "Deep residual learning for compressed sensing MRI," *2017 IEEE 14th International Symposium on Biomedical Imaging (ISBI 2017)*, 2017, pp. 15-18.
- [14] K. H. Jin, M. T. McCann, E. Froustey, M. Unser, "Deep convolutional neural network for inverse problems in imaging," in *IEEE Transactions on Image Processing*, vol. 26, no. 9, pp. 4509-4522, 2017.
- [15] G. Yang, S. Yu, H. Dong, G. Slabaugh, P. L. Dragotti, X. Ye, F. Liu, S. Arridge, J. Keegan, Y. Guo, D. Firmin, "DAGAN: Deep De-Aliasing Generative Adversarial Networks for Fast Compressed Sensing MRI Reconstruction," in *IEEE Transactions on Medical Imaging*, vol. 37, no. 6, pp. 1310-1321, 2018.
- [16] T. M. Quan, T. Nguyen-Duc and W. -K. Jeong, "Compressed Sensing MRI Reconstruction Using a Generative Adversarial Network With a Cyclic Loss," in *IEEE Transactions on Medical Imaging*, vol. 37, no. 6, pp. 1488-1497, 2018.
- [17] M. Mardani; E. Gong; J. Y. Cheng; S. S. Vasanawala; G. Zaharchuk; L. Xing; J. M. Pauly, "Deep Generative Adversarial Neural Networks for Compressive Sensing MRI," in *IEEE Transactions on Medical Imaging*, vol. 38, no. 1, pp. 167-179, 2019.
- [18] Y. Yang, J. Sun, H. Li and Z. Xu, "ADMM-CSNet: A deep learning approach for image compressive sensing," in *IEEE Transactions on Pattern Analysis and Machine Intelligence*, vol. 42, no. 3, pp. 521-538, 2020.
- [19] K. Hammernik, T. Klatzer, E. Kobler, M. P. Recht, D. K. Sodickson, T. Pock, and F. Knoll. "Learning a variational network for reconstruction of accelerated MRI data," *Magn. Reson. Med.*, vol.79, no. 6, pp. 3055-3071, 2018.
- [20] J. Zhang and B. Ghanem, "ISTA-Net: Interpretable optimization-Inspired deep network for image compressive sensing," *2018 IEEE/CVF Conference on Computer Vision and Pattern Recognition*, 2018, pp. 1828-1837.
- [21] H. K. Aggarwal, M. P. Mani, and M. Jacob, "MoDL: Model-Based deep learning architecture for inverse problems," in *IEEE Transactions on Medical Imaging*, vol. 38, no. 2, pp. 394-405, 2019.
- [22] J. Schlemper, J. Caballero, J. V. Hajnal, A. N. Price and D. Rueckert, "A Deep Cascade of Convolutional Neural Networks for Dynamic MR Image Reconstruction," in *IEEE Transactions on Medical Imaging*, vol. 37, no. 2, pp. 491-503, 2018.
- [23] T. Eo, Y. Jun, T. Kim, J. Jang, H. Lee, D. Hwang, "KIKI-net: cross-domain convolutional neural networks for reconstructing undersampled magnetic resonance images," *Magn. Reson. Med.*, vol. 80, no. 5, pp. 2188-2201, 2018.
- [24] J. Cheng, Z. Cui, W. Huang, Z. Ke, L. Ying, H. Wang, Y. Zhu, D. Liang, "Learning Data Consistency and its Application to Dynamic MR Imaging," in *IEEE Transactions on Medical Imaging*, vol. 40, no. 11, pp. 3140-3153, 2021.
- [25] D. Liang, J. Cheng, Z. Ke and L. Ying, "Deep Magnetic Resonance Image Reconstruction: Inverse Problems Meet Neural Networks," in *IEEE Signal Processing Magazine*, vol. 37, no. 1, pp. 141-151, 2020.
- [26] B. Yaman, S. A. H. Hosseini, S. Moeller, J. Ellermann, K. Uğurbil, and M. Akçakaya, "Self - supervised learning of physics - guided reconstruction neural networks without fully sampled reference data," *Magn. Reson. Med.*, vol. 84, no. 6, pp. 3172-3191, 2020.
- [27] F. Liu, R. Kijowski, G. E. Fakhri, L. Feng, "Magnetic resonance parameter mapping using model-guided self-supervised deep learning," *Magn. Reson. Med.*, vol. 85, no. 6, pp. 3211-3226, 2021.
- [28] Z. Ke, J. Cheng, L. Ying, H. Zheng, Y. Zhu, and D. Liang, "An unsupervised deep learning method for multi-coil cine MRI," *Physics in medicine & biology*, vol. 65, no. 23, pp. 235041-235041, 2020.
- [29] K. Lei, M. Mardani, J. M. Pauly and S. S. Vasanawala, "Wasserstein GANs for MR Imaging: From Paired to Unpaired Training," in *IEEE Transactions on Medical Imaging*, vol. 40, no. 1, pp. 105-115, 2021.
- [30] E. K. Cole, J. M. Pauly, S. S. Vasanawala, F. Ong, "Unsupervised MRI Reconstruction with Generative Adversarial Networks," in *28th International Society for Magnetic Resonance in Medicine (ISMRM)*, 2020. [Online].
- [31] G. Oh, B. Sim, H. Chung, L. Sunwoo and J. C. Ye, "Unpaired Deep Learning for Accelerated MRI Using Optimal Transport Driven CycleGAN," in *IEEE Transactions on Computational Imaging*, vol. 6, pp. 1285-1296, 2020.
- [32] G. Oh, J. E. Lee and J. C. Ye, "Unpaired MR Motion Artifact Deep Learning Using Outlier-Rejecting Bootstrap Aggregation," in *IEEE Transactions on Medical Imaging*, vol. 40, no. 11, pp. 3125-3139, 2021.
- [33] J. I. Tamir, S. X. Yu, M. Lustig, "Unsupervised Deep Basis Pursuit: Learning inverse problems without ground-truth data," in *27th International Society for Magnetic Resonance in Medicine (ISMRM)*, 2019, Montréal.
- [34] H. K. Aggarwal, A. Pramanik and M. Jacob, "Ensure: Ensemble Stein's Unbiased Risk Estimator for Unsupervised Learning," *ICASSP 2021 - 2021 IEEE International Conference on Acoustics, Speech and Signal Processing (ICASSP)*, 2021, pp. 1160-1164.
- [35] J. Yoo, K. H. Jin, H. Gupta, J. Yerly, M. Stuber, and M. Unser, "Time-Dependent Deep Image Prior for Dynamic MRI," in *IEEE Transactions on Medical Imaging*, vol. 40, no. 12, pp. 3337-3348, 2021.
- [36] J. Lehtinen, J. Munkberg, J. Hasselgren, S. Laine, T. Karras, M. Aittala, and T. Aila, "Noise2Noise: Learning Image Restoration without Clean Data," *Proceedings of the 35th International Conference on Machine Learning (PMLR)*, vol. 80, pp. 2965-2974, 2018.
- [37] J. Liu, Y. Sun, C. Eldeniz, W. Gan, H. An, and U. S. Kamilov, "RARE: Image Reconstruction Using Deep Priors Learned Without Groundtruth," in *IEEE Journal of Selected Topics in Signal Processing*, vol. 14, no. 6, pp. 1088-1099, 2020.
- [38] Y. Romano, M. Elad, and P. Milanfar, "The little engine that could: regularization by denoising (RED)," *Society for Industrial and Applied Mathematics Journal (SIAM) on Imaging Sciences*, vol. 10, no. 4, pp. 1804-1844, 2017.
- [39] S. V. Venkatakrisnan, C. A. Bouman, and B. Wohlberg, "Plug-and-Play priors for model based reconstruction," *2013 IEEE Global Conference on Signal and Information Processing*, 2013, pp. 945-948.
- [40] K. Zhang, W. Zuo, Y. Chen, D. Meng, and L. Zhang, "Beyond a Gaussian denoiser: Residual learning of deep CNN for image denoising," in *IEEE Transactions on Image Processing*, vol. 26, no. 7, pp. 3142-3155, 2017.
- [41] S. Boyd, N. Parikh, E. Chu, B. Peleato, and J. Eckstein, "Distributed optimization and statistical learning via the alternating direction method of multipliers," *Foundations and Trends in Machine Learning*, vol. 3, pp. 1-122, 2011.
- [42] O. Ronneberger, P. Fischer, T. Brox, "U-net: Convolutional networks for biomedical image segmentation," *Medical Image Computing and Computer-Assisted Intervention - MICCAI 2015*, p.234-241.
- [43] F. Knoll, J. Zbontar, A. Sriram, M. J. Muckley, M. Bruno, A. Defazio, M. Parente, K. J. Geras, J. Katsnelson, H. Chandarana, Z. Zhang, M. Drozdalva, A. Romero, M. Rabbat, P. Vincent, J. Pinkerton, D. Wang, N. Yakubova, E. Owens, C. L. Zitnick, M. P. Recht, D. K. Sodickson, and Y. W. Lui, "fastMRI: A publicly available raw k-space and DICOM dataset of knee images for accelerated MR image reconstruction using machine learning," *Radiology: Artificial Intelligence*, vol. 2, no. 1, e190007, 2020.
- [44] E. T. Reehorst and P. Schniter, "Regularization by denoising: Clarifications and new interpretations," in *IEEE Transactions on Computational Imaging*, vol. 5, no. 1, pp. 52-67, 2019.
- [45] V. Antun, F. Renna, C. Poon, B. Adcock, and A. C. Hansen, "On instabilities of deep learning in image reconstruction and the potential costs of AI," *Proceedings of the National Academy of Sciences - PNAS*, vol. 117, no. 48, pp. 30088-30095, 2020.